



Ceria-promoted Ni/SBA-15 catalysts for ethanol steam reforming with enhanced activity and resistance to deactivation

Di Li^a, Liang Zeng^a, Xinyu Li^a, Xiao Wang^a, Hongyan Ma^a, Suttichai Assabumrungrat^b, Jinlong Gong^{a,*}

^a Key Laboratory for Green Chemical Technology of Ministry of Education, School of Chemical Engineering and Technology, Tianjin University,

Collaborative Innovation Center of Chemical Science and Engineering, Tianjin 300072, China

^b Department of Chemical Engineering, Faculty of Engineering, Chulalongkorn University, Bangkok 10330, Thailand

ARTICLE INFO

Article history:

Received 8 January 2015

Received in revised form 10 April 2015

Accepted 10 April 2015

Available online 13 April 2015

Keywords:

Hydrogen

Ethanol steam reforming

Ceria

Ni sintering

Coke deposition

ABSTRACT

This paper describes the synthesis of CeO₂-promoted Ni/SBA-15 catalysts (denoted as CeNi/SBA-15) via a surfactant-assisted iso-volumetric impregnation method and their application in ethanol steam reforming. Various techniques including N₂ adsorption-desorption, X-ray diffraction, H₂ temperature-programmed reduction, temperature-programmed oxidation, transmission electron microscopy and thermogravimetric analysis were employed to characterize the prepared and spent catalysts. The results showed that the incorporation of CeO₂ could effectively control the particle size of Ni via strong metal-support interaction and promote the homogeneous distribution of Ni and Ce to achieve large Ni–CeO₂ interface. Consequently, the CeNi/SBA-15 catalysts exhibited superior activity with respect to the reference Ni/SBA-15 catalyst without ceria addition. The effect of ceria loading on the properties of the catalysts was also investigated, and the catalyst with Ce/Ni atomic ratio of 1 was the optimized composition owing to its strong metal-support interaction and high nickel active surface area. The ceria-promoted catalysts showed enhanced long-term stability in ethanol steam reforming. The strong interaction between Ni and CeO₂, as well as the confinement of SBA-15 support restricted the nickel particle growth under harsh reaction conditions. Additionally, the ceria promoter contributed to suppressing coke deposition effectively, which led to the enhanced coking-resistance as observed on CeNi/SBA-15 catalysts.

© 2015 Elsevier B.V. All rights reserved.

1. Introduction

With rising global demands for energy, diminishing availability of fossil fuels, and growing concerns upon pollution prevention, alternative and environmentally friendly energy sources have captured much attention in recent research. Hydrogen is a clean energy carrier and its application in proton exchange membrane fuel cells (PEMFC) for electricity generation only produces water. H₂ used in current industries is mainly obtained from fossil fuels such as natural gas, oil-derived naphtha and coal, which leads to co-production of significant amounts of greenhouse gas (GHG)CO₂ [1]. Biomass and biomass-derivatives offer renewable hydrogen sources and a theoretically closed carbon loop since CO₂ could be recycled back to plants via photosynthesis [2]. Consequently, great efforts have been undertaken to efficiently extract hydrogen from biomass, among

which ethanol steam reforming (ESR, Eq. (1)) is of great interest to chemical industries due to the high H₂ yield and the mature technology to produce ethanol from biomass [3,4].



In the past few years, the interests in developing hydrogen fuel cells have spurred extensive studies upon the ESR process, many of which focus on investigating various catalytic systems [5]. Both noble metal-based catalysts (e.g., Ru, Rh, Pd and Pt) and non-noble metal-based catalysts (Ni, Co) are found to be promising candidates for ESR reactions [6–9]. Although noble metal-based catalysts exhibit outstanding activity and stability for ESR, their utilization at large scales is limited by their high costs [10,11]. Non-noble metal-based catalysts, especially Ni-based catalysts, are widely employed in the reforming process due to their low costs, wide availability and excellent capability for C–C and C–H bond rupture [12–14]. However, Ni-based catalysts generally suffer rapid deactivation caused by sintering of active nickel species and coke deposition, which

* Corresponding author. Tel.: +86 22 27405596; fax: +86 22 87401818.

E-mail address: jlgong@tju.edu.cn (J. Gong).

remains a major challenge for developing robust Ni-based catalysts [15,16].

Enhancing the resistance to deactivation is a key issue in improving the performance and durability of Ni-based catalysts in ESR reactions [17]. Recently, controlling the sizes of nickel particles to several nanometers has been proved to be positive to inhibit the formation of surface carbonaceous species [18,19]. Chen et al. demonstrated that small Ni crystals possessed a high saturation concentration of carbon and therefore a low driving force for carbon diffusion through the nickel crystals [20]. An effective way of improving Ni dispersion and suppressing the aggregation of nickel nanoparticles is their accommodation in porous supports such as porous silica and alumina, which generally offer large surface areas and multiple pores [21,22]. Among numerous porous supports, mesoporous silica molecular sieve SBA-15 possesses a series of unique properties such as large specific surface areas, long-range ordering of mesoporous channels and thick pore walls with high hydrothermal stability, therefore it is considered as an excellent host to disperse and confine nanoparticles [23,24]. Liu et al. obtained nano-sized nickel particles with narrow distribution in Ni/SBA-15 catalysts, which gave even higher activity than Ru catalysts for ammonia decomposition [25]. A series of Cu-Ni/SBA-15 catalysts were prepared and evaluated by Vizcaino and co-workers for H₂ production via ESR [26–28]. However, it has been reported that Ni particles could diffuse out of the mesoporous channels to the outer surface of the silica support at elevated temperatures owing to the inherently weak interaction between nickel nanoparticles and the silica support, resulting in the loss of the confinement effect and subsequent sintering [23,29].

A possible solution is the utilization of promotional oxides (e.g., TiO₂, ZrO₂ and CeO₂) to strengthen the interaction with nickel nanoclusters [30–32]. Recent studies have demonstrated that CeO₂ exhibits the capability to stabilize metal particles against thermal sintering due to the strong metal-support interaction (SMSI) [33,34]. The existence of the SMSI between nickel and ceria can modify the structural and electronic properties of Ni, which contributes to high activity and stability of Ni-based catalysts [35]. Additionally, the Ni–Ce systems are generally less prone to coke deposition [36,37]. It is well established that CeO₂ has excellent oxygen storage-release capability by readily altering its oxidation states between Ce⁴⁺ and Ce³⁺ [32,38,39]. The mobile oxygen released from the lattice can react with carbonaceous species as soon as it forms and thus keep the metal surface free of carbon deposits, therefore suppressing catalyst deactivation [10,40]. It is also remarkable that Ni–CeO₂ systems show low methanation activity and high water–gas shift (WGS) activity, which is crucial to achieve high selectivity towards hydrogen via ESR reactions [41,42].

Previously, we have reported that the presence of confinement effect stabilized nickel nanoclusters against sintering while ceria addition suppressed coke deposition on the catalysts [10,15,31,43]. Therefore, it is expected that combining the two promotional strategies in ceria-promoted Ni/SBA-15 catalysts would further enhance the performance of the catalysts in steam reforming of ethanol. This paper describes a facile approach to incorporate nickel nanoparticles and ceria into the mesoporous channels of SBA-15 via a surfactant-assisted iso-volumetric impregnation method. The physical-chemical properties of the catalysts were studied by N₂-adsorption, H₂-chemisorption, H₂ temperature-programmed reduction (H₂-TPR), X-ray diffraction (XRD), transmission electron microscopy (TEM), thermogravimetric analysis (TGA) and temperature-programmed oxidation (TPO). Catalytic tests were carried out in order to evaluate the effects of ceria on the ESR performances of the catalysts. We also investigated the deactivation behaviors of the catalysts with or without ceria promotion.

2. Experimental

2.1. Catalyst preparation

xCeNi/SBA-15 catalysts in this study were prepared by a surfactant-assisted iso-volumetric impregnation method. The Ni loading was fixed to 3 wt% for all the samples investigated in the present study. By varying the amount of CeO₂ addition, the Ce/Ni atomic ratios were tuned, which were 0.25, 0.5, 1 and 2, respectively (denoted as x=0.25, 0.5, 1 and 2). Typically, SBA-15 (Nanjing JCNANO Co., Ltd) was pre-dried at 393 K for 6 h. Ni(NO₃)₂·6H₂O (99.0%, Sinopharm Chemical Reagent Co., Ltd), Ce(NO₃)₃·6H₂O (99.0%, Sinopharm Chemical Reagent Co., Ltd) and surfactant cetyltrimethylammonium bromide (CTAB, 99.0%, Sinopharm Chemical Reagent Co., Ltd) were all dissolved in absolute ethanol (99.8%, Tianjin Guangfu Fine Chemical Research Institute). The solution was then added dropwise onto the SBA-15 support. The resulting mixture was further sonicated for 0.5 h and dried in air at room temperature for 24 h. The resultant powder was finally calcined at 823 K for 2 h to achieve xCeNi/SBA-15 catalysts. The as-prepared catalysts were ground and sieved to 20–40 mesh particles for catalytic tests. A reference Ni/SBA-15 catalyst containing the same Ni content was synthesized in the absence of CeO₂ with a similar procedure.

2.2. Characterization

Surface areas and pore structures of catalysts were measured using a Micromeritics Tristar 3000 analyzer by N₂ adsorption-desorption at 77 K. Prior to the tests, all materials were degassed at 573 K for 3 h. The specific surface areas were calculated from the isotherms using the Brunauer–Emmett–Teller (BET) method, and the pore distribution and the cumulative volumes of pores were obtained by the Barret–Joyner–Halenda (BJH) method from the desorption branches of the N₂ isotherms.

Elemental composition of the prepared catalysts was determined by the inductively coupled plasma optical emission spectroscopy (ICP-OES) (VISTA-MPX, Varian). Prior to measurements, the samples were digested in HF solutions.

XRD patterns were performed with 2θ values between 10° and 85° using a Rigaku D/max-2500 diffractometer employing the graphite filtered Cu Kα radiation ($\lambda = 1.54056 \text{ \AA}$). The Scherrer's equation was used to estimate the mean Ni crystalline size based on the diffraction peaks of the Ni (1 1 1) facet.

The morphology of catalysts was characterized using a FEI Tecnai G2 F20 transmission electron microscope at 100 kV. The microscope was also equipped with devices for high-resolution electron energy-loss spectroscopy (EELS) for elemental analysis. The sample powder was first dispersed in ethanol by sonication; drops of the suspension were applied onto a copper grid-supported transparent carbon foil and dried in air.

H₂-TPR was conducted to determine the reduction behavior of the catalysts. The experiments were performed on a Micromeritics AutoChem II 2920 apparatus. Typically, a powder sample (100 mg) was pretreated at 673 K for 1 h under flowing Ar (30 mL/min) to remove any moisture and impurities. After cooling to 373 K, a flow rate of 30 mL/min of 10 vol% H₂–Ar was introduced for the reduction. Then the temperature was increased linearly from 373 K to 1173 K at a rate of 10 K/min.

Nickel active surface area was determined by H₂ pulse chemisorption (Micromeritics AutoChem II 2920). After the catalyst was reduced at 873 K for 1 h under 10% H₂/Ar flow, it was cooled down to 298 K under the Ar atmosphere, and then H₂ pulses were injected until the eluted peak area of consecutive pulses was constant. The active surface area of Ni was calculated from the volume of H₂ adsorbed by assuming an H/Ni_s (surface nickel atom)

Table 1

Textural properties of the catalysts.

Sample	BET surface area (m^2/g)	Pore volume (cm^3/g)	Ni content (wt%) ^a	Ce content (wt%) ^a	Crystal size (nm) ^b	S_H ($\text{m}^2/\text{g}_{\text{Ni}}$) ^c
Pure SBA-15	687	0.93	–	–	–	–
Ni/SBA-15	616	0.90	2.8	–	10.1/16.7	4.3
0.25CeNi/SBA-15	600	0.88	2.8	1.9	5.4	8.1
0.5CeNi/SBA-15	540	0.80	2.7	3.5	5.0	9.1
1CeNi/SBA-15	538	0.79	2.8	7.1	4.8/5.2	13.8
2CeNi/SBA-15	514	0.71	2.7	13.9	5.6	9.4

^a Determined by ICP-OES.^b Determined from Scherrer's equation from the (1 1 1) plane of Ni in XRD patterns, before stability test/after stability test.^c Nickel active surface area determined by H₂ pulse chemisorption.

stoichiometry of 1 and a surface area of $6.5 \times 10^{-20} \text{ m}^2$ per Ni atom [44].

TGA was carried out using a thermal analysis system (STA449F3, NETZSCH Corp.). The experiments were performed in a flow of air (50 mL/min) with a heating rate of 10 K/min and a final temperature of 1123 K. The amount of carbon deposition was calculated based on the mass loss profiles in TGA tests.

TPO was performed by using Micromeritics AutoChem II 2920 apparatus equipped with a HIDEN QLC-20 mass spectrometer (MS). The spent catalyst (20 mg) was pretreated at 423 K for 0.5 h under flowing Ar (30 mL/min). Upon cooling to 323 K, a flow rate of 30 mL/min of air was used for oxidation and the temperature was increased linearly from 373 K to 1173 K at a rate of 10 K/min. The CO₂ in the effluent was monitored and recorded online by MS.

2.3. Catalytic test

Catalytic activity tests were conducted at atmospheric pressure in a quartz fixed-bed tubular reactor ($\Phi 8 \times 30 \text{ mm}$) loaded with 50 mg catalysts (20–40 mesh) mixed with 1 ml of quartz particles. Prior to the test, the catalysts were reduced at 873 K for 1 h in a flow of 10 vol% H₂/N₂ (100 mL/min). The liquid solution with a specific steam-to-carbon molar ratio (S/C) of 4 was fed through an HPLC pump (P230, Elite, China) into a heated chamber (423 K) to evaporate the solution completely in the stream of N₂ (180 mL/min). The products were analyzed online by a gas chromatograph (GC, Agilent 7890A) equipped with two detectors. One is a flame ionization detector (FID) with a Porapak-Q column using N₂ as a carrier gas to analyze the organic species such as ethanol and acetaldehyde. The other one is a thermal conductivity detector (TCD) with a TDX-01 column using He as a carrier gas to monitor the incondensable gas species including hydrogen, carbon dioxide, carbon monoxide and methane.

Ethanol conversion, hydrogen selectivity and C-containing gas products selectivities were calculated as follow:

$$X_{\text{EtOH}} (\%) = \frac{F_{\text{EtOH,in}} - F_{\text{EtOH,out}}}{F_{\text{EtOH,in}}} \times 100 \quad (2)$$

$$S_{\text{H}_2} (\%) = \frac{1}{6} \times \frac{\text{moles}(\text{H}_2)\text{produced}}{\text{moles}(\text{EtOH})\text{feed} \times X_{\text{EtOH}}} \times 100 \quad (3)$$

$$S_j (\%) = \frac{(\%)j \times i}{\sum ((%)j \times i)} \times 100 \quad (4)$$

where j represents the carbon containing species in the products, including CH₄, CO, CO₂, C₂H₄, C₂H₆, CH₃CHO and CH₃COCH₃, and i is the number of carbon atoms in the carbon containing species.

The carbon balance was within $\pm 5\%$ for all catalytic runs. Data for the catalyst activity were collected when the reaction reached stable conditions, and repeated tests have been run to confirm the reproducibility of the data. It should be emphasized that according to the definitions, the sum of the selectivities of H₂ and the carbon-

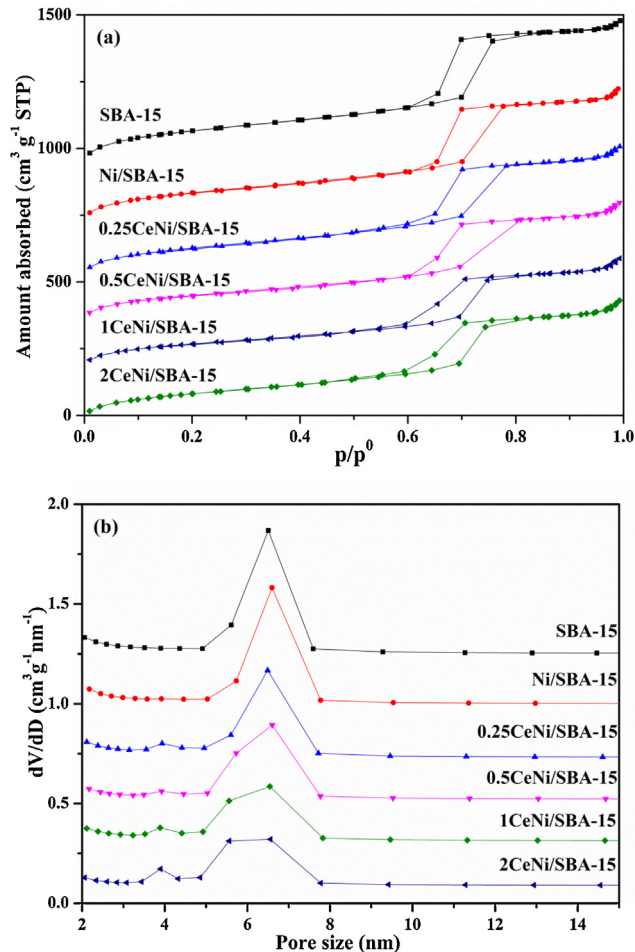


Fig. 1. (a) N₂ adsorption–desorption isotherms, (b) pore size distribution.

containing species does not lead to unity since they are calculated based on independent hydrogen and carbon balances, respectively.

3. Results and discussion

3.1. Characterization of as-prepared catalysts

The N₂ adsorption–desorption isotherms of the Ni/SBA-15 and CeNi/SBA-15 catalysts are exhibited in Fig. 1a. All the samples display type IV hysteresis loop isotherms, indicating that the mesoporous structures are largely maintained after the incorporation of nickel oxide and ceria. Pore size distribution obtained from the desorption branches of the N₂ isotherms using the BJH method reveals that SBA-15 support has narrow pore size distribution as illustrated in Fig. 1b. However, the peaks are widened as a result of the partial blockage of the primary mesopores with increasing

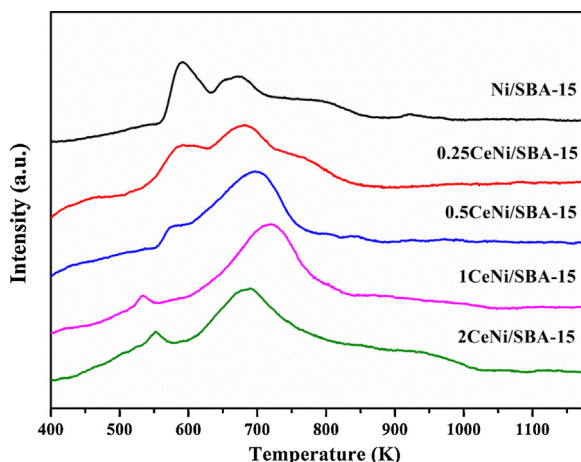


Fig. 2. TPR profiles of as-prepared Ni/SBA-15 and xCeNi/SBA-15 catalysts.

nickel oxide and ceria addition, while small mesopores centered at 3.8 nm are generated, possibly due to the accumulation of the confined particles.

Table 1 summarizes the textural properties of Ni/SBA-15 and CeNi/SBA-15 samples. Apparently, the incorporation of nickel oxide and ceria has significant impacts on the physical properties of the samples, as notable decreases in BET surface area and pore volume are observed, indicating that nickel oxide and ceria have successfully entered the pore systems. Moreover, the blockage of pore entrances by nickel oxide and/or ceria particles could also account for the decreases in surface areas and pore volumes.

H_2 -TPR technique was employed to study the reduction behavior of the catalysts as shown in Fig. 2. Three reduction peaks are present for Ni/SBA-15 at 593 K, 673 K and around 800 K, respectively. According to previous investigations, Ni^{2+} is reduced to Ni^0 without going through intermediate oxides, and therefore H_2 consumption peaks appear at different temperatures should be assigned to different species [45,46]. The sharp peak at 593 K is caused by the reduction of bulk NiO crystallites located on the external surface of SBA-15 with a weak interaction with the support, while the second one centered at 673 K could be due to the reduction of NiO nanoparticles confined within the mesopores and thus in a strong interaction with the silica support [23,47]. The broad peak at the higher temperature is likely to be the reduction of nickel phyllosilicate or nickel hydrosilicate species [25,29].

Similarly, three H_2 consumption peaks are also observed for 0.25CeNi/SBA-15 sample, assigned as NiO with weak interaction with the support, NiO with strong interaction with the support and Ni silicates, respectively. Compared with the Ni/SBA-15 catalyst, the first peak shifts towards lower temperatures, indicating that smaller NiO clusters are formed outside the silica matrix and easier to be reduced [48,49]. On the other hand, the intensity of the second H_2 consumption peak in xCeNi/SBA-15 catalysts becomes stronger when ceria loading increases, and the corresponding temperature also moves towards higher temperatures. The lower extent of reducibility is caused by the strengthened interaction between NiO and CeO_2 , which is crucial for obtaining sintering-resistant Ni particles during the calcination and reduction process.

For xCeNi/SBA-15 catalysts, a shoulder peak corresponding to Ni silicates is observed exclusively for 0.25CeNi/SBA-15. It is noteworthy that a broad reduction peak from 800 K to 1023 K is detected for 2CeNi/SBA-15, which is likely due to the reduction of bulk CeO_2 at high ceria loading [50].

Diffraction patterns of reduced Ni/SBA-15 and xCeNi/SBA-15 catalysts are presented in Fig. 3a. The broad peaks originated from about $2\theta=15^\circ$ to 35° are the reflection peaks of the SiO_2

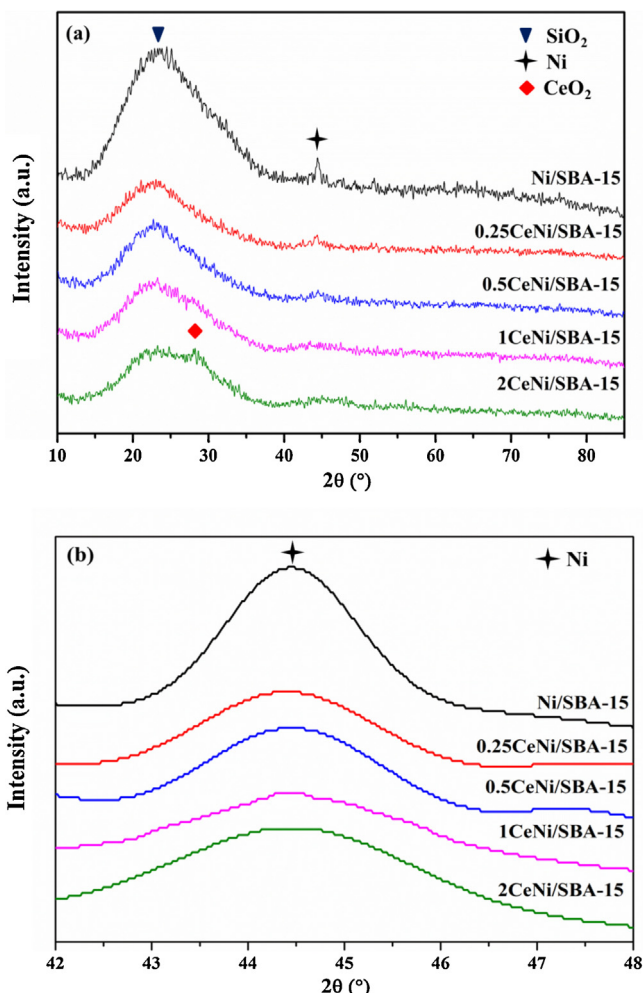


Fig. 3. (a) XRD patterns of the reduced catalysts. (b) Magnified view of the XRD patterns between 42° and 48° for the reduced catalysts.

frameworks of SBA-15 support [51]. For all the samples, the reflection peaks at $2\theta=44.5^\circ$, which can be assigned as the characteristic peaks of metallic Ni , can be observed in the XRD patterns. The reflection peaks of Ni^0 for xCeNi/SBA-15 catalysts are less obvious than that for the Ni/SBA-15 catalyst, suggesting that the Ni^0 particles are smaller and highly dispersed in the presence of CeO_2 (Fig. 3b). This could be attributed to the formation of $Ni-Ce$ mixed oxide due to strong interaction between NiO and CeO_2 and/or the dilution effect caused by CeO_2 addition to separate Ni particles and thus suppress their aggregation during the reduction [51–53]. Moreover, it has also been reported that nickel crystallites could spread over the CeO_2 at $Ni-CeO_2$ interface under reducing atmosphere and elevated temperatures and be stabilized by the strong metal-support interaction, therefore improving Ni dispersion [54,55]. The diffraction peaks of CeO_2 are not observed until the Ce/Ni atomic ratio increases to 2, revealing CeO_2 is either amorphous or well-dispersed in the catalysts. Note that a peak corresponding to CeO_2 is found at $2\theta=28.5^\circ$ for 2CeNi/SBA-15 as the evidence of bulk CeO_2 at higher CeO_2 loading. This is in line with the results from TPR. According to results of H_2 chemisorption (Table 1), the aggregation of ceria could be negative for the exposure of nickel, possibly due to its blockage of the mesopores or coverage over accessible nickel active sites [56]. Carrera Cerritos et al. demonstrated that the coverage of lanthanum over Ni could lower the accessibility of Ni surface to the gas phase [57]. It was also reported that Ni/CeO_2 underwent surface reconstruction to partially bury Ni inside

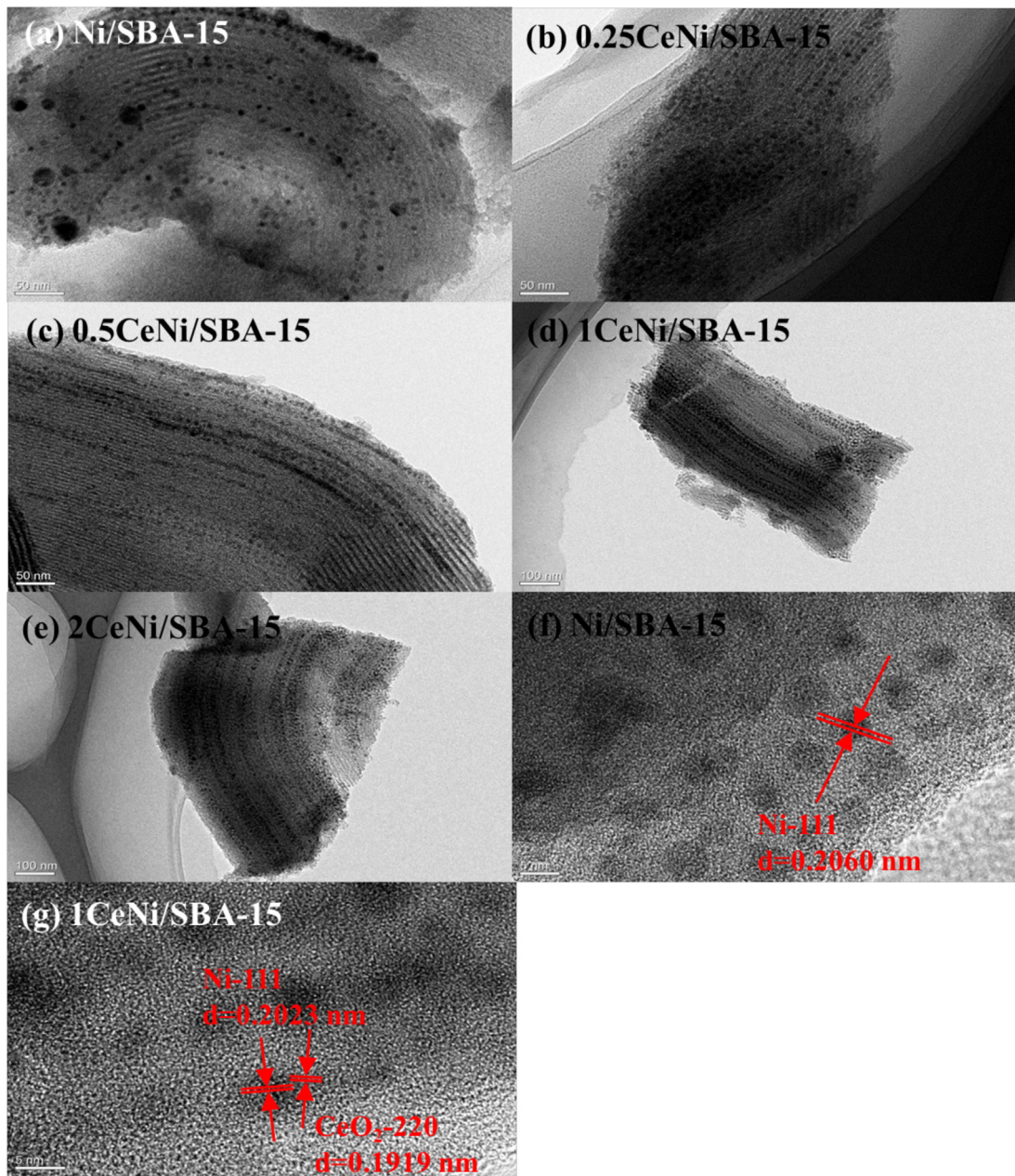


Fig. 4. TEM images of reduced (a,f) Ni/SBA-15 (b) 0.25CeNi/SBA-15 (c) 0.5CeNi/SBA-15 (d,g) 1CeNi/SBA-15 (e) 2CeNi/SBA-15 catalysts.

CeO₂ bulk under reducing atmosphere [58,59]. Consequently, the 1CeNi/SBA-15 exhibits the smallest Ni particle size and the highest Ni active surface area.

Fig. 4 shows the TEM micrographs of the reduced catalysts. Clearly, spherical nickel particles are uniformly incorporated in the ordered mesoporous channels of SBA-15 in all ceria-modified catalysts (Fig. 4b–e). The xCeNi/SBA-15 catalysts prepared by the surfactant-assisted impregnation method had nano-sized nickel particles aligned within the mesoporous channels of SBA-15, showing a better nickel dispersion than those reported previously [60,61]. Additionally, the Ni and ceria particles were distinguished using lattice fringe identification on the HRTEM image (Fig. 4g). The Ni particle with *d*-spacing of 0.202 nm was associated with (1 1 1) Ni plane (JCPDS 87-0712), while the ceria particle with *d*-spacing of 0.192 nm was related to the (2 2 0) ceria plane (JCPDS 81-0792). A close contact between Ni and ceria particles was observed. Although well-dispersed Ni particles are also observed

in the channels of SBA-15 (Fig. 4a and f), some large Ni particles are formed outside the mesopores in the Ni/SBA-15 catalyst, which is in agreement with the results from XRD patterns. This suggests that some nickel particles may migrate from the channels to the external surface of SBA-15 support and sinter during reduction at 873 K. Such phenomena were previously reported for the reduction of NiO particles inserted in SBA-15 and SBA-16 [62]. Nevertheless, in CeO₂-promoted samples, the enhanced interaction between Ni and CeO₂ inhibits the tendency of Ni to migrate and agglomerate at elevated temperatures [34]. Therefore, all xCeNi/SBA-15 catalysts retain their excellent nickel dispersions after reduction, consistent with the observations in XRD and H₂-chemisorption.

In order to investigate the interaction and interfacial area between Ni and CeO₂, EELS mapping technique is adopted. The composition map obtained by overlapping the Ni and Ce maps is shown in Fig. 5. The green and the red pixels represent the nickel and cerium element distributions, respectively. The yellow area

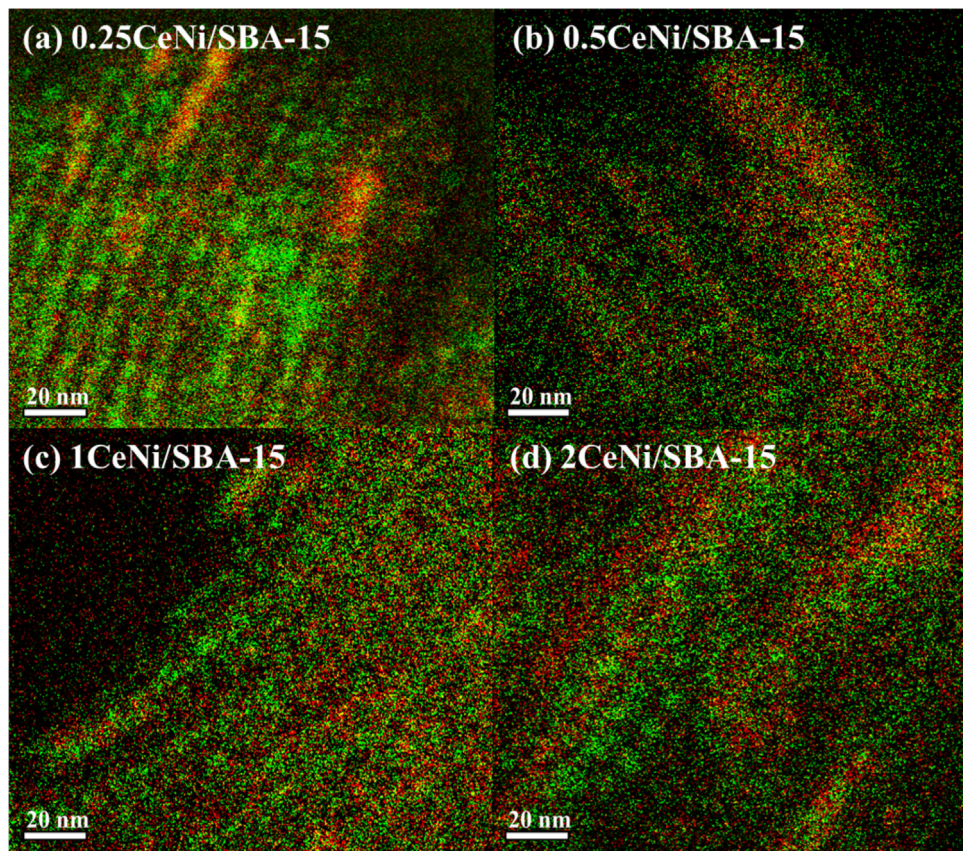


Fig. 5. EELS mapping of reduced xCeNi/SBA-15 catalysts, with green pixels for Ni element and red pixels for Ce element. (a) 0.25CeNi/SBA-15 (b) 0.5CeNi/SBA-15 (c) 1CeNi/SBA-15 (d) 2CeNi/SBA-15. (For interpretation of the references to color in this figure legend, the reader is referred to the web version of this article.)

could be attributed to a homogeneous mixture of the two elements, indicating the interfacial area between Ni and CeO₂. It can be seen that small nickel particles are uniformly aligned along the channels, confirming the high dispersion of Ni particles. Ceria, amorphous or in the form of very small particles, which is hard to identify, is well-overlapped with the nickel particles. For Ce/Ni = 0.25, the yellow area is small, whereas larger areas of yellow region are found on samples with Ni/Ce = 2 and 1, suggesting the homogeneous Ni–Ce element distribution in the catalysts. However, when the amount of CeO₂ further increases to Ce/Ni = 2, large areas of separated red region and green particles emerged. This indicates that excessive CeO₂ tends to aggregate instead of interacting with nickel particles, therefore decreasing the interface between Ni and CeO₂. As a result, the best Ni–CeO₂ interaction was found for 1CeNi/SBA-15 catalyst due to the large interfacial area. EELS mapping provides fundamental evidence for the difference of Ni–CeO₂ interface among the CeO₂-promoted samples.

3.2. ESR activity test

ESR activity results are illustrated in Fig. 6. Major products are H₂, CO, CO₂, CH₄ and CH₃CHO for all the catalysts in the study. It can be clearly seen that all the CeO₂-promoted catalysts exhibited higher ethanol conversion, higher H₂ selectivity as well as lower aldehyde selectivity than the Ni/SBA-15 catalyst. It could be related to larger active nickel surface areas of the xCeNi/SBA-15 with respect to Ni/SBA-15 due to the dispersing effect of CeO₂, as Ni is identified as the active center for C–C and C–H bond cleavage, which facilitates the conversion of ethanol and other C₂ intermediates [63,64].

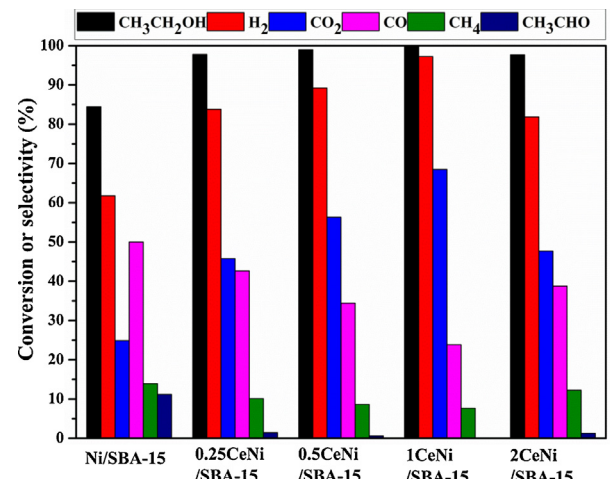
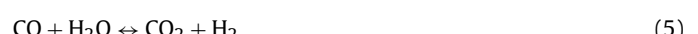


Fig. 6. ESR activity of the catalysts. Reaction conditions: S/C = 4, 923 K, 1 atm, W/F ratio = 1.7 g h/mol, ethanol in gas 4.2 vol%. Time on stream: 3 h.

The methanation and WGS reaction are the main side reactions in ESR, affecting the product distribution significantly as shown in Eqs. (5) and (6), respectively [65]. Methanation is highly undesirable since it consumes H₂. In the present study, the CH₄ selectivity was low for all the samples investigated, indicating that methanation was suppressed under the reaction conditions due to its extremely exothermic nature.



With the introduction of CeO₂, significant enhancement in H₂ selectivity was achieved, accompanied by higher CO₂ selectivity and lower CO selectivity. Since the CO₂/CO ratio has been considered as an indicator for WGS activity, the enhanced H₂ production with CeO₂ addition is probably associated with the promotion of the catalysts' capability to facilitate WGS reaction [66,67]. It is well known that CeO₂-containing catalysts show higher selectivity for H₂ and CO₂ in steam reforming reactions [68]. CeO₂ has excellent redox property and high oxygen storage capacity, and therefore its presence can contribute to water activation [67,69]. The OH groups dissociated from water over CeO₂ efficiently eliminate absorbed CO and produce H₂ simultaneously.

Recently, Rodriguez's group investigated the ESR over a Ni/CeO₂ extensively to elucidate the role of the catalyst under reaction conditions [70]. They have demonstrated that Ni metal in close contact with CeO₂ serves as the active phase for the steam reforming reactions. Specifically, metallic Ni helps in the adsorption of ethanol and in the scission of its C–C bond, while oxygen vacancies in CeO₂ are responsible for the activation of water to generate OH groups, which in turn react with C_xH and C_xO_yH intermediate species to produce CO₂ and H₂. Similar reaction scheme has also been proposed by Shen and co-workers for Ir/CeO₂ catalysts in ESR and Rh/CeO₂ catalysts in autothermal reforming of ethanol, concluding that the reforming reaction mainly occurred at the metal-CeO₂ interface [71,72]. As shown in Fig. 6, the H₂ yield and CO₂ selectivity gradually increases as the Ce/Ni ratio increases to 1, whereas a sharp decrease in H₂ yield and CO₂ selectivity is observed for catalyst when Ce/Ni ratio further increases to 2. The 1CeNi/SBA-15 catalyst with an optimal Ni/Ce ratio gave complete ethanol conversion and highest hydrogen selectivity (97%), followed by 0.5CeNi/SBA-15 catalyst, which can be attributed to their large metal-ceria interfaces as evidenced by HRTEM and EELS mapping.

3.3. ESR stability test

Generally, the ESR is considered as a severe reaction under harsh conditions and significant deactivation has been reported regardless of the metal and support utilized [5]. Therefore, catalyst stability is one of the key issues in the development of efficient catalysts for H₂ production via steam reforming of ethanol. To further investigate the promotional effect of CeO₂, stability tests have been performed to study the long-term catalytic performance of the catalysts. Fig. 7 illustrates the 50 h catalytic performances of the selected catalysts and the deactivation behaviors for different catalysts are distinguishable. For Ni/SBA-15 catalyst (Fig. 7a), the conversion of ethanol continuously declined during reaction together with increasing selectivity of aldehyde, indicating that the catalyst's ability to facilitate C–C bond cleavage was weakened. The initial H₂ selectivity was 65% and followed a downwards trend to 45% eventually. Both CO selectivity and CH₄ selectivity were high, which could be ascribed to the low activity of WGS reaction and relatively high activity of methanation. With CeO₂ addition, 1CeNi/SBA-15 showed great enhancement in catalytic stability as it maintained 90% ethanol conversion even after 50 h on stream with only traceable amount of C₂ byproduct (Fig. 7b). The hydrogen selectivity suffered a sharp decline in the initial 3 h and then decreased very slowly and finally reached steady state at 80%. The selectivity of CO₂ consisted with the trend of H₂, accompanied by the rise of the selectivity of CO. Obviously, the 1CeNi/SBA-15 catalyst exhibited stable and efficient hydrogen production during the reaction, whereas Ni/SBA-15 catalyst produced less hydrogen with more C₂ byproduct due to incessant degradation of activity. Generally, active metal sintering and coke deposition are the primary causes for catalyst deactivation in ESR, and both will be investigated.

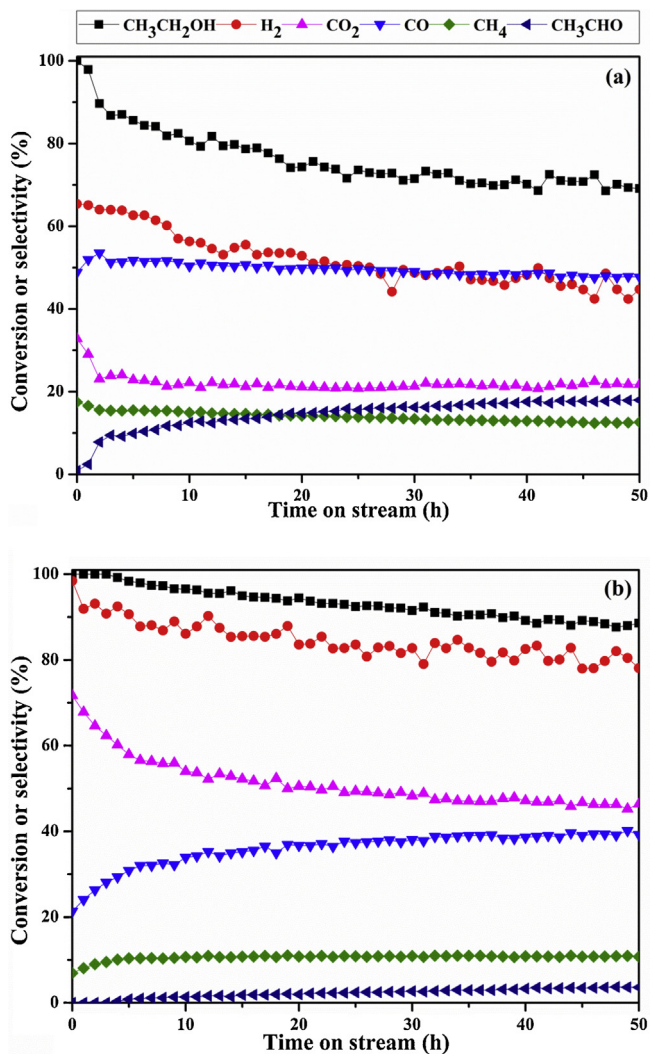


Fig. 7. Stability of the catalysts. (a) Ni/SBA-15 (b) 1CeNi/SBA-15. Reaction conditions: S/C = 4, 923 K, 1 atm, W/F ratio = 1.5 g h/mol, ethanol in feed 4.5 vol%.

3.4. Characterization of spent catalysts

Various characterization techniques were conducted in order to understand the origin of catalyst deactivation and their difference in deactivation behavior. First of all, the XRD patterns of the two spent catalysts are provided in Fig. 8. The reflection peak of graphite ($2\theta = 26.4^\circ$) is detected for both catalysts. The graphite peak of Ni/SBA-15 is more intense than that of 1CeNi/SBA-15, evidencing that carbon deposition is much more significant on Ni/SBA-15 catalyst. Furthermore, the attenuated reflection peak of Ni shows that the Ni/SBA-15 catalyst suffered from sintering, and the nickel particle size increased to ~ 16.7 nm after the stability test. The sintered Ni particles led to reduced active metal surface, thus resulting in weakened capability towards C–C bond cleavage, which is responsible for the loss of ethanol conversion and the concomitant formation of aldehyde as shown in Fig. 7a. On the other hand, the crystal size of Ni remained intact (~ 5.2 nm) for the spent 1CeNi/SBA-15 catalyst, and its peak assigned to coke deposition is less obvious.

TGA investigations of the spent catalysts were carried out to determine the amount of carbon deposition quantitatively. As the mass loss profiles shown in Fig. 9, the mass started decreasing from 650 K and reached unchanged at 940 K. It should be noted that no mass gain was observed since the nickel loading (3 wt%) was quite low. Apparently, the accumulated amount of coke deposition on

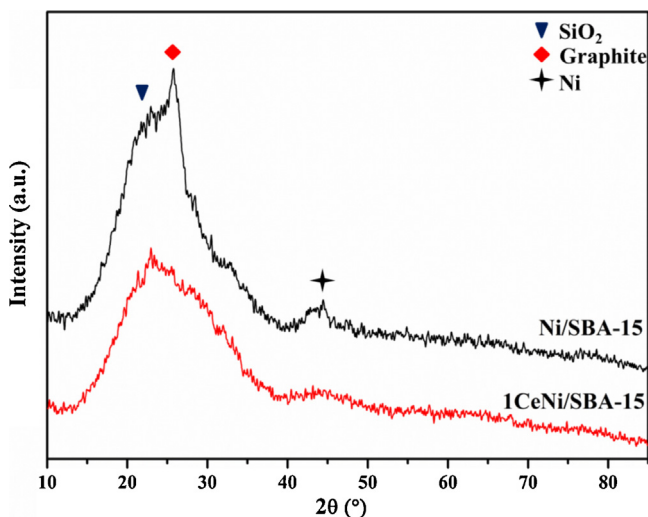


Fig. 8. XRD patterns of the spent catalysts.

spent 1CeNi/SBA-15 is 8%, which, however, was quadrupled on the spent Ni/SBA-15 catalyst (32%). TPO was utilized to confirm the order, and the concentration of CO₂ was detected and recorded by MS as shown in Fig. 10. Both curves are normalized and the peak

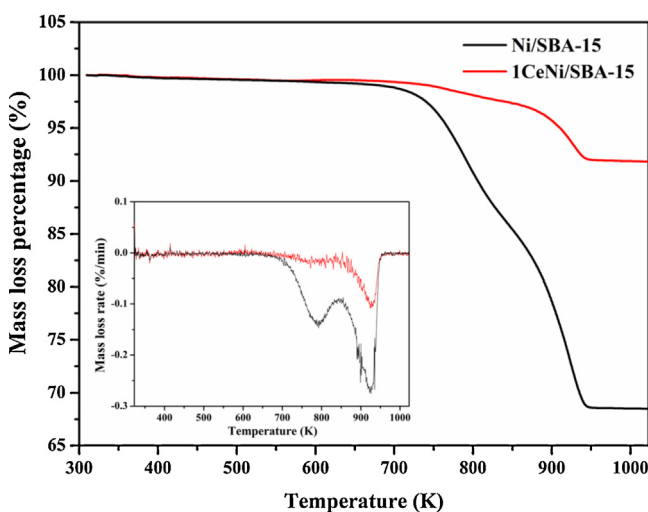


Fig. 9. TGA profiles and DTG profiles (inset) for the spent catalysts.

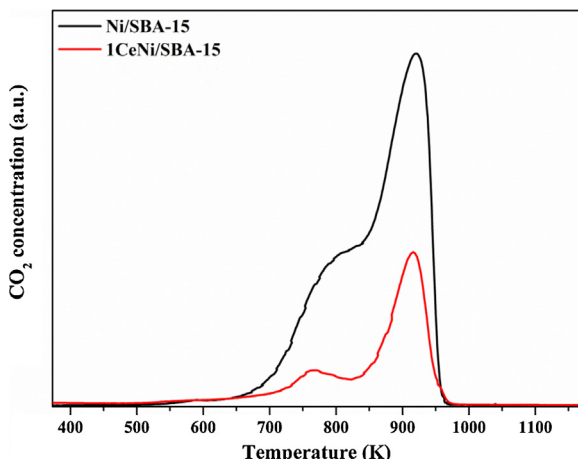


Fig. 10. TPO profiles of the spent catalysts.

area corresponds to the amount of carbon deposition. By quantifying the peak areas, the area ratio of 1CeNi/SBA-15 to Ni/SBA-15 was calculated to be 0.3. The difference between the two spent catalysts in the amount of coke deposition acquired from TPO is in close agreement with that obtained from TGA. The observation illustrates that carbon deposition on the catalyst surface was effectively suppressed for CeO₂-promoted Ni/SBA-15 catalyst.

Moreover, we could notice the presence of two peaks of CO₂ production in the TPO spectra, corresponding to two distinct carbonaceous species on the used catalyst surface. Note that two peaks are also found in DTG profiles (Fig. 9inset). The existence of two different kinds of coke species has been reported previously [73,74]. It is generally assumed that the first peak at lower temperatures is related to coke deposited on the metal surface, while the second peak at higher temperatures could be due to coke deposited on the support [65,75,76]. Coke deposited on nickel surface significantly decreases the accessibility of active nickel sites for reforming reaction, thus resulting in degradation of catalyst activity. The low-temperature peak on spent 1CeNi/SBA-15 has lower intensity and smaller peak area compared to that on used Ni/SBA-15, indicating that less coke deposition is present on Ni surface. Additionally, the first CO₂ production peak of 1CeNi/SBA-15 shifts towards lower temperatures by 20 K as compared to that of Ni/SBA-15. This reveals that the coke deposited on CeO₂-promoted catalyst is more reactive and easily removed by oxidation. Combining TGA, TPO and XRD, we are able to conclude that 1CeNi/SBA-15 catalyst possesses lower amounts of coke deposition after the stability test, and more importantly, less coke deposited on the active metal, evidencing its anti-coking ability with CeO₂ addition, which accounts for the excellent long-term stability during ethanol steam reforming reaction.

Fig. 11 displays TEM images recorded after 50 h ESR stability tests on selected catalysts. The spent catalysts gave evidently different appearances due to the formation of carbonaceous species. Spent Ni/SBA-15 catalyst was seriously encapsulated by deposited carbon, where filamentous carbon was clearly presented in the sample as well (Fig. 11a). This is in line with the XRD patterns since intensive reflection peak of graphite was detected in Ni/SBA-15 after the stability test. Although coke deposition has also been noticed on spent 1CeNi/SBA-15 catalyst, the amount of coke deposition was less and therefore the catalyst kept mainly exposed (Fig. 11c). Sanchez-Sanchez et al. demonstrated that the formation of carbon filaments was significantly suppressed due to the interaction between metallic Ni particles and ceria or lanthana species [77]. Beyond carbon deposition, no obvious Ni particle growth was found for used 1CeNi/SBA-15 catalyst, revealing its excellent sintering resistance (Fig. 11d). However, considerable Ni particle growth to ~20 nm was observed for Ni/SBA-15 catalyst, and sintered Ni particles were found outside the mesopores of the silica support and completely encapsulated by carbon deposition (Fig. 11b). It should be noted that some nickel particles located on the external surface of the SBA-15 upon reduction (Fig. 4a), and these Ni particles with weak interaction with the silica support were susceptible to sintering and coke deposition under reaction conditions.

Coke deposition as well as active metal sintering is generally considered to be the primary culprits for catalyst deactivation in ethanol steam reforming [16]. The main routes for coke formation are the polymerization of ethylene derived from ethanol dehydration (Eq. (7)), methane dehydrogenation (Eq. (8)) and CO disproportionation (Boudouard reaction, Eq. (9)). [78]. Since ethylene



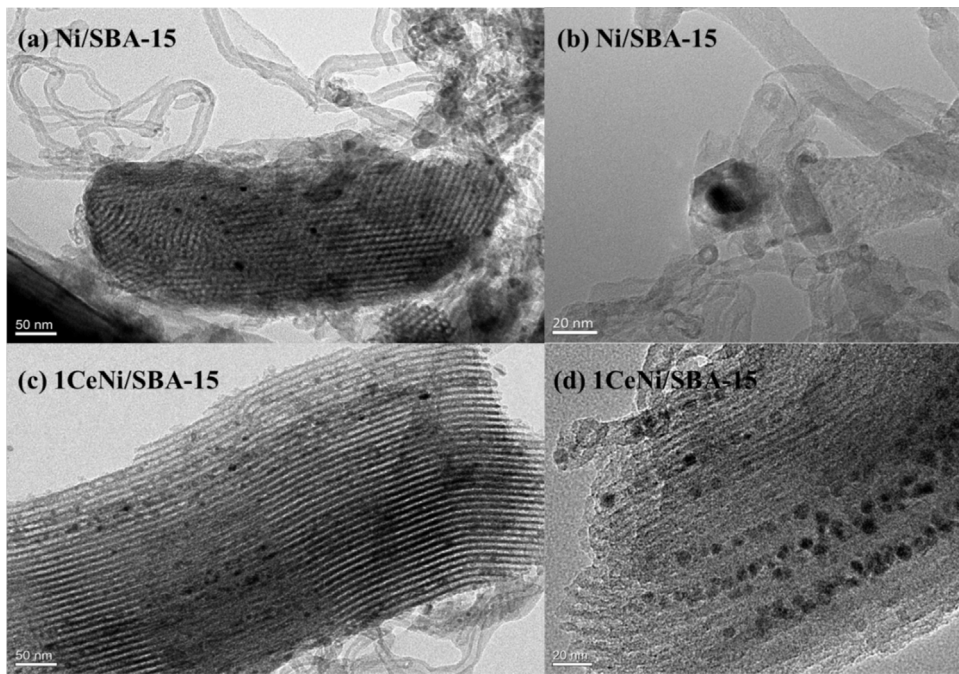


Fig. 11. TEM images of the spent (a,b) Ni/SBA-15 catalyst and (c,d) 1CeNi/SBA-15 catalyst.

is not detected in our study, methane dehydrogenation and Boudouard reaction are the possible routes for carbon deposition on Ni/SBA-15 and xCeNi/SBA-15 catalysts [70]. Yang et al. reported that electrons released from the oxygen vacancies in CeO₂ could migrate through the Ni–CeO₂ interface to the unfilled *d*-orbital of Ni⁰, and thus the electron-rich property of Ni⁰ could effectively inhibit the decomposition of CH₄ [79]. According to Senanayake et al., the strong electronic perturbation induced by ceria on Ni reduced the ability of Ni to break C–O bonds, which could probably suppress the activity of CO disproportionation to produce carbon deposits [35]. Additionally, in the presence of steam, the OH groups generated on CeO₂ contribute to remove the coke precursor such as methyl groups to produce CO, CO₂ and H₂ [70]. It has been reported that the high oxygen storage and transport capacity of CeO₂ enables a carbon removal mechanism that takes place at the metal–ceria interface [33,76,80]. The highly mobile oxygen in ceria can instantaneously react with carbon species formed during the reaction and maintain a clean metal surface, and the oxygen vacancies are readily replenished by steam from the feed [77,81,82]. The addition of ceria promoter not only reduces the rate of carbon deposition but also accelerates the rate of coke gasification, therefore enhancing the stability of the 1CeNi/SBA-15 catalyst.

In the case of Ni/SBA-15, the weak interaction between Ni and SiO₂ carrier is negative to the stability of the catalyst as the Ni particles migrated from the mesoporous channels of SBA-15 to the external surface of the support at elevated temperatures, which led to severe Ni aggregation and catalyst deactivation eventually. The nickel particle size is closely associated to coke deposition, as large particle size is highly favored by coking [20,83,84]. As a result, the catalytic performance of Ni/SBA-15 was greatly deteriorated due to severe sintering and simultaneous coking. Nevertheless, the strong interaction between nickel and ceria effectively stabilized the Ni⁰ particles and thus kept the well-dispersed morphology of Ni in 1CeNi/SBA-15 catalyst, as evidenced by XRD and TEM. The anchoring effect of CeO₂ for metal particles via SMSI has been demonstrated for various metal–ceria systems including Ni–CeO₂, Ir–CeO₂, Rh–CeO₂ and Ag–CeO₂ [34,71,72,85,86]. Consequently, the sintering-resistant 1CeNi/SBA-15 catalyst maintained its large

active metal surface as well as sufficient Ni–CeO₂ interface, exhibiting excellent catalytic performance during 50 h on stream.

4 Conclusions

In summary, we have successfully prepared a series of CeO₂-promoted Ni/SBA-15 catalysts by a surfactant-assisted iso-volumetric impregnation method and evaluated their performances in ethanol steam reforming. Compared with Ni/SBA-15, the incorporation of CeO₂ effectively controlled the size of nickel particles via SMSI, leading to well-dispersed nickel particles confined in the mesoporous channels of SBA-15. The CeNi/SBA-15 catalysts possessed homogeneous Ni–Ce distribution, and the increased Ni–CeO₂ interface obviously enhanced their catalytic performances. The 1CeNi/SBA-15 catalyst with optimized Ni/Ce atomic ratio exhibited the highest activity in ESR, owing to its highest nickel active surface area and largest Ni–CeO₂ interfacial area.

In addition, coke deposition and nickel metal sintering were the primary culprits for catalyst deactivation, both of which were significantly suppressed on CeO₂-promoted catalysts. Specifically, the strong interaction between nickel particles and ceria, together the confinement of SBA-15 support, retained the small nickel particle size (5.2 nm), revealing the excellent sintering-resistance of the CeO₂-promoted catalysts. On the other hand, the ceria promoter inhibited the coke formation on catalyst surface and facilitated the removal of coke deposition simultaneously. Therefore, the CeNi/SBA-15 catalysts exhibited efficient and stable hydrogen production via ESR for 50 h on stream.

Acknowledgments

This work was supported by the National Science Foundation of China (21,006,068, 21,222,604, 21,206,115 and 21,376,169), the Program for New Century Excellent Talents in University (NCET-10-0611), the Scientific Research Foundation for the Returned Overseas Chinese Scholars (MoE), and the Program of Introducing Talents of Discipline to Universities (B06006).

References

- [1] V. Nichele, M. Signoretto, F. Menegazzo, I. Rossetti, G. Cruciani, *Int. J. Hydrogen Energy* 39 (2014) 4252–4258.
- [2] I.I. Soykal, H. Sohn, U.S. Ozkan, *ACS Catal.* 2 (2012) 2335–2348.
- [3] J. Sun, Y. Wang, *ACS Catal.* 4 (2014) 1078–1090.
- [4] J. Zhang, Z. Zhong, X.M. Cao, P. Hu, M.B. Sullivan, L. Chen, *ACS Catal.* 4 (2013) 448–456.
- [5] L.V. Mattos, G. Jacobs, B.H. Davis, F.B. Noronha, *Chem. Rev.* 112 (2012) 4094–4123.
- [6] X. Wu, S. Kawi, *Energy Environ. Sci.* 3 (2010) 334–342.
- [7] L. Coronel, J.F. Múnera, A.M. Tarditi, M.S. Moreno, L.M. Cornaglia, *Appl. Catal. B* 160–161 (2014) 254–266.
- [8] I. Rossetti, J. Lasso, V. Nichele, M. Signoretto, E. Finocchio, G. Ramis, A. Di Michele, *Appl. Catal. B* 150–151 (2014) 257–267.
- [9] J. Sun, A.M. Karim, D. Mei, M. Engelhard, X. Bao, Y. Wang, *Appl. Catal. B* 162 (2015) 141–148.
- [10] C. Zhang, S. Li, M. Li, S. Wang, X. Ma, J. Gong, *AIChE J.* 58 (2012) 516–525.
- [11] V. Palma, F. Castaldo, P. Ciambelli, G. Iaquaniello, *Appl. Catal. B* 145 (2014) 73–84.
- [12] G.W. Huber, J.W. Shabaker, J.A. Dumesic, *Science* 300 (2003) 2075–2077.
- [13] V. Nichele, M. Signoretto, F. Pinna, F. Menegazzo, I. Rossetti, G. Cruciani, G. Cerrato, A. Di Michele, *Appl. Catal. B* 150 (2014) 12–20.
- [14] A.L.M. da Silva, J.P. den Breejen, L.V. Mattos, J.H. Bitter, K.P. de Jong, F.B. Noronha, *J. Catal.* 318 (2014) 67–74.
- [15] C. Zhang, S. Li, G. Wu, J. Gong, *Catal. Today* 233 (2013) 53–60.
- [16] J. Sehested, *Catal. Today* 111 (2006) 103–110.
- [17] S. Li, J. Gong, *Chem. Soc. Rev.* 43 (2014) 7245–7256.
- [18] D. Baudouin, U. Rodemerck, F. Krumeich, A.d. Mallmann, K.C. Szeto, H. Ménard, L. Veyre, J.-P. Candy, P.B. Webb, C. Thieuleux, C. Copéret, *J. Catal.* 297 (2013) 27–34.
- [19] J.-H. Kim, D.J. Suh, T.-J. Park, K.-L. Kim, *Appl. Catal. A* 197 (2000) 191–200.
- [20] D. Chen, K.O. Christensen, E. Ochoa-Fernández, Z. Yu, B. Tøtdal, N. Latorre, A. Monzón, A. Holmen, *J. Catal.* 229 (2005) 82–96.
- [21] A. Cao, R. Lu, G. Veser, *Phys. Chem. Chem. Phys.* 12 (2010) 13499–13510.
- [22] S. Qiu, X. Zhang, Q. Liu, T. Wang, Q. Zhang, L. Ma, *Catal. Commun.* 42 (2013) 73–78.
- [23] A. Ungureanu, B. Dragoi, A. Chiriac, C. Ciotonea, S. Royer, D. Duprez, A.S. Mamede, E. Dumitriu, *ACS Appl. Mater. Interfaces* 5 (2013) 3010–3025.
- [24] G. Prieto, J. Žečević, H. Friedrich, K.P. de Jong, P.E. de Jongh, *Nat. Mater.* 12 (2013) 34–39.
- [25] H. Liu, H. Wang, J. Shen, Y. Sun, Z. Liu, *Appl. Catal. A* 337 (2008) 138–147.
- [26] A. Carrero, J.A. Calles, A.J. Vizcaino, *Appl. Catal. A* 327 (2007) 82–94.
- [27] A.J. Vizcaino, A. Carrero, J.A. Calles, *Catal. Today* 146 (2009) 63–70.
- [28] M. Lindo, A.J. Vizcaino, J.A. Calles, A. Carrero, *Int. J. Hydrogen Energy* 35 (2010) 5895–5901.
- [29] S. Zhang, S. Muratsugu, N. Ishiguro, M. Tada, *ACS Catal.* 3 (2013) 1855–1864.
- [30] R. Burch, A.R. Flambard, *J. Catal.* 78 (1982) 389–405.
- [31] S. Li, C. Zhang, Z. Huang, G. Wu, J. Gong, *Chem. Commun.* 49 (2013) 4226–4228.
- [32] Y. Zhou, J. Zhou, *J. Phys. Chem. C* 116 (2012) 9544–9549.
- [33] J. Carrasco, L. Barrio, P. Liu, J.A. Rodriguez, M.V. Ganduglia-Pirovano, *J. Phys. Chem. C* 117 (2013) 8241–8250.
- [34] X. Du, D. Zhang, L. Shi, R. Gao, J. Zhang, *J. Phys. Chem. C* 116 (2012) 10009–10016.
- [35] S.D. Senanayake, J.A. Rodriguez, D. Stacchiola, *Top. Catal.* 56 (2013) 1488–1498.
- [36] L. Jalowiecki-Duhamel, C. Pirez, M. Capron, F. Dumeignil, E. Payen, *Catal. Today* 157 (2010) 456–461.
- [37] S. Natesakhawat, R.B. Watson, X. Wang, U.S. Ozkan, *J. Catal.* 234 (2005) 496–508.
- [38] I.I. Soykal, H. Sohn, D. Singh, J.T. Miller, U.S. Ozkan, *ACS Catal.* 4 (2014) 585–592.
- [39] X. Liu, K. Zhou, L. Wang, B. Wang, Y. Li, *J. Am. Chem. Soc.* 131 (2009) 3140–3141.
- [40] Z. Ferencz, A. Erdőhelyi, K. Baan, A. Oszkó, L. Óvári, Z. Konya, C. Papp, H.-P. Steinrück, J. Kiss, *ACS Catal.* 4 (2014) 1205–1218.
- [41] M.L. Ang, U. Oemar, E.T. Saw, L. Mo, Y. Kathiraser, B.H. Chia, S. Kawi, *ACS Catal.* 4 (9) (2014) 3237–3248.
- [42] S. Senanayake, J. Evans, S. Agnoli, L. Barrio, T.-L. Chen, J. Hrbek, J. Rodriguez, *Top. Catal.* 54 (2011) 34–41.
- [43] C. Zhang, W. Zhu, S. Li, G. Wu, X. Ma, X. Wang, J. Gong, *Chem. Commun.* (2013).
- [44] C.H. Bartholomew, R.B. Pannell, *J. Catal.* 65 (1980) 390–401.
- [45] C. Louis, Z.X. Cheng, M. Che, *J. Phys. Chem.* 97 (1993) 5703–5712.
- [46] W.-S. Dong, H.-S. Roh, K.-W. Jun, S.-E. Park, Y.-S. Oh, *Appl. Catal. A* 226 (2002) 63–72.
- [47] N. Wang, W. Chu, T. Zhang, X.S. Zhao, *Int. J. Hydrogen Energy* 37 (2012) 19–30.
- [48] Y. Li, B. Zhang, X. Xie, J. Liu, Y. Xu, W. Shen, *J. Catal.* 238 (2006) 412–424.
- [49] X.-Y. Quek, D. Liu, W.N.E. Cheo, H. Wang, Y. Chen, Y. Yang, *Appl. Catal. B* 95 (2010) 374–382.
- [50] H.V. Fajardo, L.F.D. Probst, N.L.V. Carreño, I.T.S. Garcia, A. Valentini, *Catal. Lett.* 119 (2007) 228–236.
- [51] H. Liu, H. Wang, J. Shen, Y. Sun, Z. Liu, *Catal. Today* 131 (2008) 444–449.
- [52] D.K. Kim, K. Stöwe, F. Müller, W.F. Maier, *J. Catal.* 247 (2007) 101–111.
- [53] W. Shan, M. Luo, P. Ying, W. Shen, C. Li, *Appl. Catal. A* 246 (2003) 1–9.
- [54] J. Beckers, G. Rothenberg, *Green Chem.* 12 (2010) 939–948.
- [55] V.M. Gonzalez-DelaCruz, J.P. Holgado, R. Pereñiguez, A. Caballero, *J. Catal.* 257 (2008) 307–314.
- [56] D. Liu, X.Y. Quek, W.N.E. Cheo, R. Lau, A. Borgna, Y. Yang, *J. Catal.* 266 (2009) 380–390.
- [57] R.I. Carrera Cerritos, R. Fuentes Ramírez, A.F. Aguilera Alvarado, J.M. Martínez Rosales, T.S. Viveros García, I.R. Galindo Esquivel, *Ind. Eng. Chem. Res.* 50 (2011) 2576–2584.
- [58] A. Caballero, J.P. Holgado, V.M. Gonzalez-delaCruz, S.E. Habas, T. Herranz, M. Salmeron, *Chem. Commun.* 46 (2010) 1097–1099.
- [59] M. Yu, Y.-A. Zhu, Y. Lu, G. Tong, K. Zhu, X. Zhou, *Appl. Catal. B* 165 (2015) 43–56.
- [60] K. Wang, X. Li, S. Ji, X. Shi, J. Tang, *Energy Fuels* 23 (2008) 25–31.
- [61] J.A. Calles, A. Carrero, A.J. Vizcaino, *Micropor. Mesopor. Mater.* 119 (2009) 200–207.
- [62] D. Kantorovich, L. Haviv, L. Vradman, M.V. Landau, *Stud. Surf. Sci. Catal.* 156 (2005) 147–154.
- [63] S.M. Gates, J.N. Russell Jr, J.T. Yates Jr, *Surf. Sci.* 171 (1986) 111–134.
- [64] J. Xu, X. Zhang, R. Zenobi, J. Yoshinobu, Z. Xu, J.T. Yates Jr, *Surf. Sci.* 256 (1991) 288–300.
- [65] A.N. Fatsikostas, X.E. Verykios, *J. Catal.* 225 (2004) 439–452.
- [66] S.M. Kim, S.I. Woo, *ChemSusChem* 5 (2012) 1513–1522.
- [67] J. Carrasco, D. López-Durán, Z. Liu, T. Duchón, J. Evans, S.D. Senanayake, E.J. Crumlin, V. Matolín, J.A. Rodríguez, M.V. Ganduglia-Pirovano, *Angew. Chem. Int. Ed.* 54 (2015) 3917–3921.
- [68] S.M. de Lima, A.M. da Silva, L.O. da Costa, U.M. Graham, G. Jacobs, B.H. Davis, L.V. Mattos, F.B. Noronha, *J. Catal.* 268 (2009) 268–281.
- [69] X. Wang, J.A. Rodriguez, J.C. Hanson, D. Gamarría, A. Martínez-Arias, M. Fernández-García, *J. Phys. Chem. B* 110 (2005) 428–434.
- [70] W. Xu, Z. Liu, A.C. Johnston-Peck, S.D. Senanayake, G. Zhou, D. Stacchiola, E.A. Stach, J.A. Rodriguez, *ACS Catal.* 3 (2013) 975–984.
- [71] W. Cai, F. Wang, A.C. Van Veen, H. Provendier, C. Mirodatos, W. Shen, *Catal. Today* 138 (2008) 152–156.
- [72] W. Cai, F. Wang, E. Zhan, A. Vanveen, C. Mirodatos, W. Shen, *J. Catal.* 257 (2008) 96–107.
- [73] P. Gallezot, C. Leclercq, J. Barbier, P. Marecot, *J. Catal.* 116 (1989) 164–170.
- [74] A.C. Basagiannis, X.E. Verykios, *Appl. Catal. A* 308 (2006) 182–193.
- [75] S. Wang, G.Q.M. Lu, *Appl. Catal. B* 16 (1998) 269–277.
- [76] S.M. Stagg-Williams, F.B. Noronha, G. Fendley, D.E. Resasco, *J. Catal.* 194 (2000) 240–249.
- [77] M.C. Sanchez-Sánchez, R.M. Navarro, J.L.G. Fierro, *Int. J. Hydrogen Energy* 32 (2007) 1462–1471.
- [78] C. Zhang, H. Yue, Z. Huang, G. Wu, S. Li, X. Ma, J. Gong, *ACS Sustainable Chem. Eng.* 1 (2013) 161–173.
- [79] R. Yang, C. Xing, C. Lv, L. Shi, N. Tsubaki, *Appl. Catal. A* 385 (2010) 92–100.
- [80] M.C.J. Bradford, M.A. Vannice, *Appl. Catal. A* 142 (1996) 73–96.
- [81] A.M. da Silva, K.R. de Souza, L.V. Mattos, G. Jacobs, B.H. Davis, F.B. Noronha, *Catal. Today* 164 (2011) 234–239.
- [82] E. Ramírez-Cabrera, A. Atkinson, D. Chadwick, *Appl. Catal. B* 47 (2004) 127–131.
- [83] K.O. Christensen, D. Chen, R. Lødeng, A. Holmen, *Appl. Catal. A* 314 (2006) 9–22.
- [84] Y. Wang, J. Peng, C. Zhou, Z.-Y. Lim, C. Wu, S. Ye, W.G. Wang, *Int. J. Hydrogen Energy* 39 (2014) 778–787.
- [85] B.C. Zhang, W.J. Cai, Y. Li, Y.D. Xu, W.J. Shen, *Int. J. Hydrogen Energy* 33 (2008) 4377–4386.
- [86] J.A. Farmer, C.T. Campbell, *Science* 329 (2010) 933–936.